Exact Force Vector Regulation of the Three-Pole Magnetic Bearing

Nicholas R. Hemenway and Eric L. Severson, ECE Department, University of Wisconsin-Madison

Abstract—The three-pole magnetic bearing is an attractive alternative to conventional four and eight pole magnetic bearings because of its simple structure and ability to be operated with three-phase power electronics. However, accurately controlling the three-pole bearing is significantly more complicated. Conventional control implementations are prone to large force vector errors that can lead to instability in the magnetic suspension system. This paper proposes a new control implementation for externally-biased three-pole bearings that eliminates force vector error. This control implementation is based on solving a fourth order polynomial in the form of a depressed quartic to determine coil current commands. An analytic framework and graphic techniques are developed to study the solution space for the bearing's coil currents and explain discontinuities that can arise in certain bearing designs. It is shown that bearings with either no bias or a normalized bias field in excess of $\frac{1}{3}$ are preferred for suspension stability. The exact force vector regulator is experimentally demonstrated in a bearing prototype and shown to be advantageous over the conventional regulation approach.

Index Terms—Magnetic bearing, magnetic suspension, electric motor, feedback control

NOMENCLATURE

α	Bearing force vector angle.
$B_{c,i}$	Control field in front of pole <i>i</i> .
$B'_{c,i}$	Normalized control field, $= B_{c_i}/B_{\text{max}}$.
$B_i^{c,\iota}$	Total airgap field in front of pole i .
$B_{ m max}$	Maximum allowable bearing airgap field.
B_0	Bearing bias field present in each airgap.
b'_x, b'_y	x, y control field space vector components
\circ_x, \circ_y	normalized by B_{max} .
Λ	Discriminant of a fourth order polynomial.
F_{max}	Maximum achievable force that any of the
1 max	•
	three poles can produce.
F_x, F_y	x, y components of a bearing force vector.
F'_x, F'_y	Normalized force components, $= F_x/F_{\text{max}}$.
\mathbf{F}'	Complex force vector normalized by F_{max} .
$i_{c,i}$	Control current flown into coil i.
i_{α}, i_{β}	α , β -axis currents of a current space vector.
k_1	Proportionality factor relating fields to forces.
k_2	Proportionality factor relating coil currents to
	airgap fields.
p, q, r	Quadratic, linear, constant coefficient of a
	fourth order polynomial.
Ċ	Non-dimensional bias field, $= B_0/B_{\text{max}}$.
>	Tion different class field, 20/2 max.

I. INTRODUCTION

Active magnetic bearings (AMBs) have the potential to overcome several limitations of conventional mechanical-type

This work was supported in part by USA National Science Foundation under Grant #1942099

bearings. Whereas contact-type bearings limit the motor system lifetime and result in substantial friction losses for high-speed operation, active magnetic bearings have no moving parts or mechanical contacts, yielding highly efficient operation, improved system longevity, and controllable rotor dynamics. These qualities are particularly desired in compressor applications, where AMBs are used in natural gas transportation, HVAC chillers, and wastewater aeration systems [1]–[3].

Radial magnetic bearings have been developed into mature commercial products as four- and eight-pole bearings [4]. Recently, three-pole bearings have been developed at research universities, for example: [5]-[20], primarily motivated by their ability to be operated by a three phase inverter and ease of manufacturing (all of which reduce cost). The wide variation of three-pole design topologies was reviewed in [5] which concludes that designs can be categorized by whether a bias field is used and whether zero-sequence currents are used in the control coils. Options for the bias field include heteropolar airgap fields, i.e. [6]-[10] and homopolar airgap fields, i.e. [17]–[20] (several of which are also able to create axial forces) as well as no bias field, i.e. [14]-[16]. The operating principles of all three-pole bearing topologies can be derived from Fig. 1, which has three electromagnetic actuators separated spatially by 120 degrees that can each impart a force on the rotor.

Three-pole bearings that use an external bias field suffer from large force vector error (often referred to as "interference forces") [9], [10], [21], [22] which reduces the bearing's stability [23]. In previous work [5], the authors have shown that 1) the force density of a three-pole bearing can be increased by 15% by using an optimal external bias field; 2) it is possible to eliminate the force vector error from externally-biased bearings by determining the necessary coil currents from a more detailed force-current model. To date, there has been no investigation into operating a three-pole bearing with the new approach for eliminating force vector error.

The main contribution of this paper is to develop, implement, and experimentally validate a so-called "exact force vector regulator" for an externally biased three-pole magnetic bearing. This paper first investigates discontinuities in the commanded coil currents that can arise from a direct implementation of the new current calculation technique. It is shown that if these issues are not properly addressed, the exact force vector regulator can introduce new bearing stability challenges into the magnetic suspension system. The paper then develops a complete implementation of the exact force vector regulator. Finally, the proposed regulator is investigated and validated through a simulation study and an experimental prototype of a combined radial axial magnetic bearing (CRAMB).

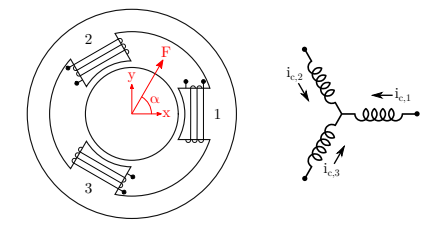


Fig. 1. Three-pole AMB and Wye coil connection used in this paper.

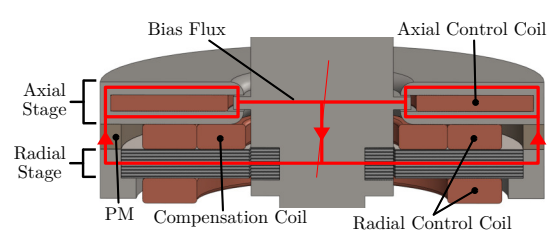


Fig. 2. Combined radial-axial magnetic bearing that uses permanent magnets to generate an external bias field for the three-pole bearing.

II. THREE-POLE AMB STRUCTURE AND FORCE MODEL

This paper assumes the three pole bearing structure depicted in Fig. 1 is operated by the conventional three phase inverter typical of electric motor drives. The coils are connected in a Wye configuration, requiring that their currents sum to zero. In addition to airgap "control" fields created by the coil currents, this paper assumes that an external flux source provides a bias field to the airgap. An example configuration is shown in Fig. 2, which depicts a combined radial-axial magnetic bearing (CRAMB) utilizing axially-magnetized permanent magnets to generate the bias flux. The "radial stage" is implemented as the three-pole bearing of Fig. 1. This particular topology is discussed at length in [24]. Other common geometry configurations to realize this are reviewed in a previous work by the authors [5], which also developed a generalized force model for the three-pole bearing and proposed an "exact solution" to calculate the currents necessary to create a desired force vector. These results form the basis of the present paper and are now summarized in this section.

Radial forces produced on the bearing's shaft can be modeled by (1). Here, \mathbf{F}' is a complex force vector normalized by the maximum force $F_{\text{max}} = k_1 B_{\text{max}}^2$ that each bearing pole can produce, $B_{c,i}$ is the control component of the airgap field in front of each pole (proportional to the pole coil's control current $i_{c,i}$), B_{max} is the maximum allowable airgap field, and $\mathrm{SV}(\vec{v})$ is a space-vector operator that operates on a cartesian vector \vec{v} as $\mathrm{SV}(\vec{v}) = [1, a, a^2] \vec{v}$, where $a = e^{\frac{j2\pi}{3}}$. The total airgap field in front of any pole is modeled as (2), which consists of $B_{c,i}$ and the bias field B_0 .

$$\mathbf{F}' = \frac{F_x + jF_y}{F_{\text{max}}} = \text{SV}(\vec{B}_c'^2) + 2\zeta \text{SV}(\vec{B}_c')$$
(1)
$$\vec{B}_c' = \frac{1}{B_{\text{max}}} [B_{c,1}, B_{c,2}, B_{c,3}]^T$$

$$B_i = B_0 + B_{c,i}$$
(2)
$$= B_0 + k_2 i_{c,i}$$

$$\zeta = \frac{B_0}{B_{\text{max}}} \tag{3}$$

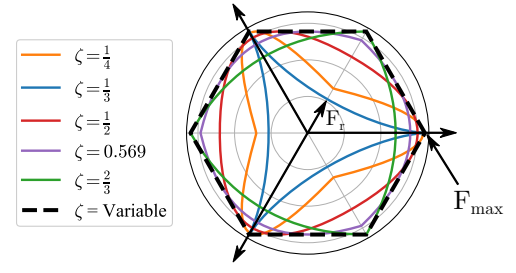


Fig. 3. Maximum force profiles for various bias field values.

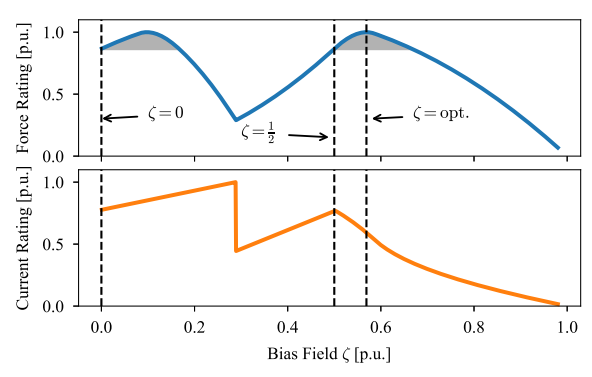


Fig. 4. Normalized rated force and current requirement profiles as a function of the bias field ζ . Shaded regions depict the margin of improvement that results from using an optimal bias field over conventional values.

When the force model for the bearing is presented in this form, it is evident that the bearing's force characteristic depends only on $F_{\rm max}$ and ζ (which depend on the bearing's geometry and materials, as described [5]). This allows for a general analysis of the bearing, decoupled from the specifics of an individual design. Note that this model assumes linear material properties and thus $F_{\rm max}$ is expected to be within the linear region of the materials. Non-dimensional results in this paper are obtained by setting $k_1=k_2=B_{\rm max}=1$. This means that control fields and currents can be used interchangeably–see (2).

It is shown in [5] that when ζ is allowed to vary, each of the bearing's three poles can produce force independently, allowing the bearing to produce forces anywhere within the dashed hexagonal profile of Fig. 3. However, when ζ is held to a fixed value (i.e., using magnets as the external flux source for the bias field, as is assumed in this paper), the maximum force in any particular direction is limited to one of the inner contours of Fig. 3. These contours each have a different force rating F_r , which is defined as the minimum force magnitude on the maximum force profile. An example rated force vector is labeled in Fig. 3 for $\zeta = \frac{1}{3}$. The design choice of ζ clearly has significant implications for the force rating of bearings with otherwise equivalent geometry (equivalent F_{\max} and therefore B_{max} values). Using an optimal bias field ($\zeta = 0.569$) can improve the three-pole bearing's force rating by 15.5% and decrease its Ampere-turn requirements by 23.4% (see [5]) compared to the bearing bias values of $\zeta = 0$ or $\zeta = \frac{1}{2}$ that are typically used. Fig. 4 highlights this result by showing the normalized force rating (blue curve) and Ampere-turn requirements (orange curve) of the three-pole bearing as a function of the bias field ζ . Section III-D will show that the ACCEPTED FOR PUBLICATION IN IEEE TRANSACTIONS ON INDUSTRY APPLICATIONS NOV/DEC 2021

For control purposes, the inverse of (1) is needed; that is, a calculation of currents required to produce a desired force vector. The traditional approach linearizes (1) about a zerocurrent operating point [9], [12], [22] and results in significant

optimal bias field has additional desired features.

force vector error. This paper uses a method proposed in [5] that inverts (1) exactly using the following procedure:

1) Solve the roots of (4). This polynomial is a depressed quartic-solution procedures are discussed in Section IV-A.

$$b'_{x} + jb'_{y} = SV(\vec{B}'_{c})$$

$$b''_{x} + pb''_{x} + qb'_{x} + r = 0$$

$$p = -3F'_{x} - 27\zeta^{2}$$

$$q = 18F'_{x}\zeta + 54\zeta^{3}$$

$$r = -27F'_{x}\zeta^{2} - \frac{9F''_{y}}{4}$$
(4)

2) Solve for b'_u as (5).

$$b_y' = \frac{3F_y'}{2(3\zeta - b_x')} \tag{5}$$

3) Solve for the three-phase control currents using (6).

$$i_{\alpha} + ji_{\beta} = \frac{B_{\text{max}}}{k_{2}} \left(b'_{x} + jb'_{y} \right)$$

$$\begin{bmatrix} i_{c,1} \\ i_{c,2} \\ i_{c,3} \end{bmatrix} = \begin{bmatrix} \frac{2}{3} & 0 \\ -\frac{1}{3} & \frac{\sqrt{3}}{3} \\ -\frac{1}{2} & -\frac{\sqrt{3}}{2} \end{bmatrix} \begin{bmatrix} i_{\alpha} \\ i_{\beta} \end{bmatrix}$$

$$(6)$$

Inspection of (5) shows there is a singularity at $b'_x = 3\zeta$. However, substitution of $b'_x = 3\zeta$ into (4) yields that this situation can only occur when $F_y = 0$. This corner case can be evaluated by taking a limit, resulting in (7).

$$b_y' = \sqrt{27\zeta^2 - 3F_x'} \tag{7}$$

The equations presented in this section form the basis of the exact force vector regulator proposed in Section III. It should be noted that the equations all assume a centered rotor, which is premised on the assumption that the position regulator can effectively control the rotor. The extension of these equations to a displaced rotor is beyond the scope of this paper.

III. EXACT FORCE VECTOR REGULATOR

This paper proposes an exact force vector regulator for the three-pole bearing by utilizing the coil current calculations of (4)–(6). The purpose of this regulator is to eliminate the error found in the conventional three-pole bearing force regulator (referred to as the "linear force regulator" as it uses a linearized force model to calculate coil currents) between the force vector that the bearing's position regulator commands and the force vector that is actually created on the shaft. By doing this, the exact force vector regulator has the potential to improve bearing stability (considered later, in Section V-A).

This section develops the exact force vector regulator approach used to select a set of bearing coil currents, investigates the solution space of (4)–(6) to showcase challenges with realizing the regulator, and develops a framework for analyzing these challenges based on the system's discriminant. Conclusions drawn from this framework inform the design of the three-pole bearing (specifically, the suitable bearing bias level ζ). It is shown that careful consideration must be given to the implementation of (4)–(6) in order to prevent excessive losses due to unnecessarily large coil currents and introducing new stability issues into the bearing's position regulator due to discontinuities in the commanded bearing currents.

3

A. Bearing Coil Current Calculations

The bearing current calculation method of (4)–(6) involves solving the roots of the fourth order polynomial (4). This means that there will be four sets of three-phase currents that are capable of producing any desired force vector. The coil currents (and therefore the ohmic losses) can vary significantly between solutions. Further complicating the solution selection is that depending on the commanded force vector, some of the solutions can be invalid-requiring either an airgap field in excess of $B_{\rm max}$ or complex (non-physical) values of current. It is proposed that for any desired force, the exact force vector regulator select a valid (physically realizable) solution with the lowest coil losses. This can be determined by selecting the current set with the lowest Euclidean L^2 norm.

The variation between solutions can be depicted by studying the example of commanding a zero force vector ($F'_x = F'_y =$ 0). Equation (4) and (5) are solved to find the four solutions of b'_x and b'_y as $(8)^1$.

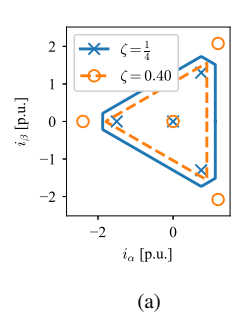
$$(b'_x, b'_y) = (0, 0)$$

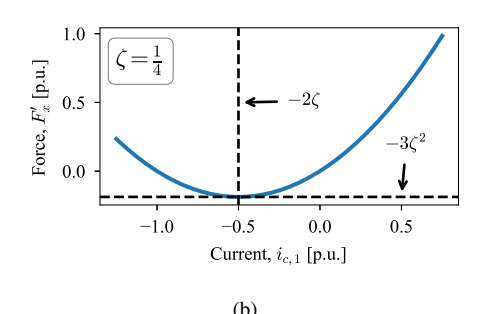
= $(-6\zeta, 0)$
= $(3\zeta, \pm 3\sqrt{3}\zeta)$ (8)

For non-zero values of ζ , three of the four solutions will require flowing current while producing no actual force. Depending on the value of ζ , this current can be quite significant. This is undesirable as it leads to additional losses and power draw from the bearing's drive. Fig. 5a depicts these zero-force locations as the blue x's and orange o's for two different values of ζ . The solid and dashed bounding regions indicate the upper limits for i_{α} and i_{β} ; any coordinates outside of the bounding regions will cause an airgap to exceed B_{max} . It can be seen that for the case of $\zeta = 0.4$, three of the four solutions require pushing the airgap fields past saturation to produce the zeroforce vector, and are therefore not valid solutions.

As the commanded force vector is swept across a bearing's realizable force profile (see Fig. 3), this broad variation in solution values and feasibility can result in the proposed exact force vector regulator commanding abrupt changes (discontinuities) in the coil currents, even for smooth force profiles. An illustrative example of discontinuities can be found by studying the geometrically simple case of producing a variable magnitude force along the x-axis. In this case, $\vec{i}_c = \frac{B_{\text{max}}}{k_2} [B'_{c,1}, -\frac{B'_{c,1}}{2}, -\frac{B'_{c,1}}{2}]^T$ is the minimum L^2 solution.

¹Since $B_{\text{max}} = k_2 = 1$, this is equivalent to i_{α} and i_{β} of the control current space vector: $\mathrm{SV}(\vec{i}_c)=i_{\alpha}+ji_{\beta}=i_{c,1}+ai_{c,2}+a^2i_{c,3},$ see (6).





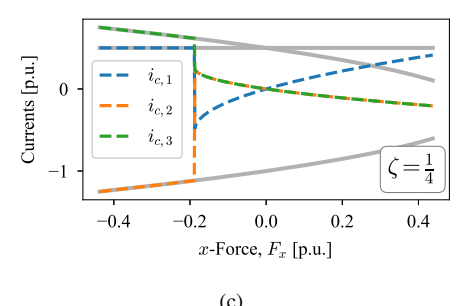


Fig. 5. (a) Four current solutions to create $F_x' = F_y' = 0$ for two bearing bias levels. Creating an x-axis force: (b) limited force capability of the minimum L^2 solution (9) and (c) the current command discontinuity when crossing $F_x' = -3\zeta^2$; grey curves depict the non-minimum L^2 solution.

Substituting this into (1) yields (9), which is a scalar quadratic equation in $i_{c,1}$. Recall that $B_{\text{max}} = k_2 = 1$ so that $\vec{i}_c = \vec{B}'_c$.

$$F_x' = \frac{3}{4}i_{c,1}^2 + 3\zeta i_{c,1} \tag{9}$$

Fig. 5b depicts (9) for a bearing biased at $\zeta=\frac{1}{4}$ and shows that a minimum force of $F'_x=-3\zeta^2$ occurs at $i_{c,1}=-2\zeta$. As the regulator requests an increasingly negative force, this solution will work until $F'_x=-3\zeta^2$ is reached. At this point, the solution's required coil currents will become complex (and therefore invalid) and the exact force vector regulator will jump to a different solution, causing a discontinuity in the commanded currents. This behavior is depicted in Fig. 5c where the bearing current discontinuity corresponds to the minimum of Fig. 5b (forces to the right of the discontinuity are created by the low power solution discussed above).

Discontinuous current commands like those shown in Fig. 5c are problematic as they are not physically realizable. At the point of discontinuity, the current slew rate will be limited by the voltage rating of the bearing drive and the coil inductance. During the transition period between the two solutions, large force vector errors will result, possibly causing the system to go unstable. The stability implications of this are investigated in Section V-A for an example bearing.

B. Analysis of Bearing Coil Current Solution Space

An analysis framework is now constructed to explain discontinuities that arise in the exact force regulator's commanded bearing currents (i.e., Fig. 5c). The framework applies to any three-pole bearing design (combination of ζ and F_{max}) for any arbitrary desired force vector within a bearing's realizable force profile (Fig. 3). The analysis framework draws from the mature body of literature on quartic polynomials and is based on evaluating the discriminant of (4). Relevant mathematical background on how the solutions to quartics relate to properties of their discriminant can be found in numerous publications and textbooks, such as [25], [26].

The discriminant Δ of (4) can be calculated as (10) in terms of the desired force components F'_x and F'_y .

$$\Delta = 2916F_{y}^{'2} \left(-F_{x}^{'4} + 24F_{x}^{'3}\zeta^{2} - 2F_{x}^{'2}F_{y}^{'2} - 162F_{x}^{'2}\zeta^{4} - 72F_{x}^{'}F_{y}^{'2}\zeta^{2} - F_{y}^{'4} - 162F_{y}^{'2}\zeta^{4} + 2187\zeta^{8} \right)$$
(10)

The sign of the discriminant determines the types of roots (coil current solutions) that will result. A negative discriminant

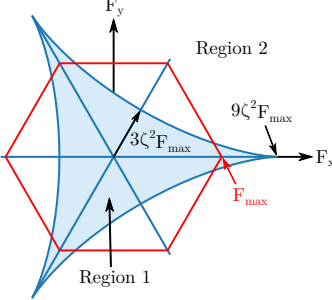


Fig. 6. The blue region denotes where the discriminant is positive and indicates that all four quartic solutions will be real valued.

indicates that there will be two distinct real roots and two complex roots. Complex roots correspond to invalid coil current solutions, meaning that F_x' and F_y' combinations which yield a negative discriminate will have only two valid sets of bearing coil currents. A positive discriminant indicates that all four solutions will either be real (all coil current solutions are valid) or complex (no coil current solutions are valid). The case of a positive discriminant can be further refined by evaluating the polynomials (11), if both polynomials are less than zero, all four solutions will be real. Finally, a zero discriminant indicates that the polynomial has a multiple root.

$$P = -24F'_x - 216\zeta^2$$

$$D = -144(F'^2_x + F'^2_y) - 4320F'_x\zeta^2 - 11664\zeta^4$$
 (11)

Regions in the F'_x - F'_y plane with different discriminant signs are depicted in Fig. 6 with the maximum profile of the three-pole bearing (Fig. 3) imposed on top. Equations (10) and (11) can be used to show that when a force vector is commanded within each of these regions, the exact force regulator will have a differing number of solutions as follows:

- 1) Blue shaded region: four valid current solutions, $\Delta > 0$ and the polynomials of (11) are negative.
- 2) Outside the blue shaded region: two valid current solutions, $\Delta < 0$.

The solid blue lines indicate edge cases, where $\Delta=0$. Interestingly, the region with four valid solutions (blue region) is completely defined in terms of the two generalized bearing design parameters ζ and $F_{\rm max}$.

It can be shown numerically that for any three-pole bearing design, a single solution of (4) will have the minimum L^2 norm (lowest power) over the entirety of region 1 and that this

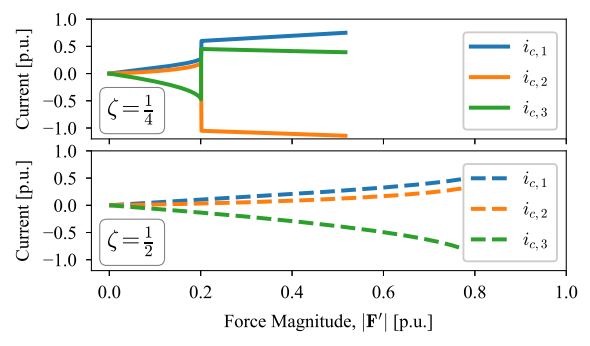


Fig. 7. Current waveform that results when commanding a variable magnitude force at an angle of $\alpha=40^\circ$ for bearings biased at $\zeta=\frac{1}{4}$ and $\zeta=\frac{1}{2}$.

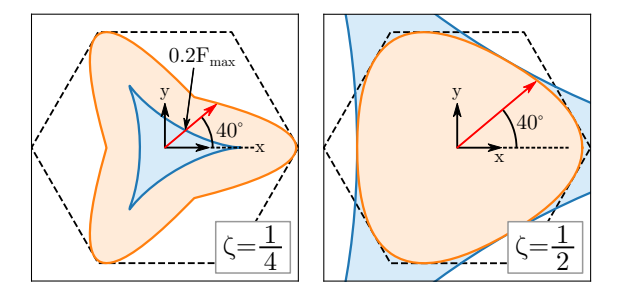


Fig. 8. Variable force magnitude command trajectory on top of two bearings' maximum force profile and discriminant regions. These plots explain current discontinuities in Fig. 7.

solution will be infeasible (complex) in region 2. This result indicates that for smooth force trajectories within region 1, the exact force regulator will command smooth coil currents (no discontinuities). However, when a force vector crosses from region 1 to region 2, the exact force vector regulator will command problematic discontinuous currents because the minimum L^2 solution will become infeasible at the boundary between regions 1 and 2. Finally, in region 2, the solution with the lowest L^2 norm will change when crossing a solid blue line at 60° , 180° , and 300° for bearings with $\zeta>0$. This will create discontinuous current commands at these angles.

C. Case Studies of Bearing Coil Current Discontinuities

Examples are now presented using the analysis framework developed in Section III-B to examine the coil current commands for different bearing designs and force trajectories.

- 1) Force along x-axis: The example considered in Section III-A and depicted in Fig. 5b and 5c is analyzed. A current discontinuity was observed for an x-axis force crossing $F_x' = -3\zeta^2$, where the minimum L^2 solution becomes infeasible for lower force values. This matches the interface of regions 1 and 2 in Fig. 6, where the analysis framework expects a current discontinuity to exist (the lowest L^2 solution is infeasible in region 2, but viable in region 1).
- 2) Variable magnitude force at 40° : In Fig. 7, the exact force vector regulator's control currents are computed for a variable magnitude force at an angle of 40 degrees for two different bias values ($\zeta = \frac{1}{4}$ and $\zeta = \frac{1}{2}$). The two curves extend to different force magnitudes because the two bearings have different force capability curves per [5] and Fig. 3.

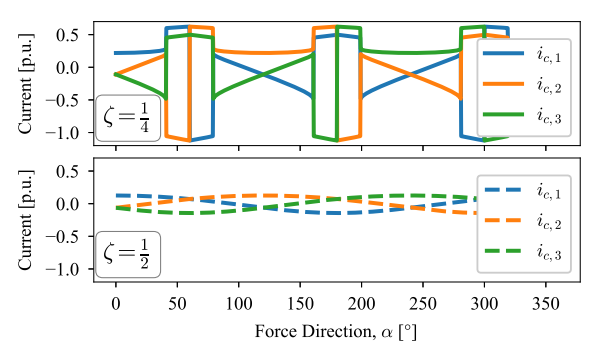


Fig. 9. Current waveform that results when commanding a force of $0.2F_{\rm max}$ in all force directions.

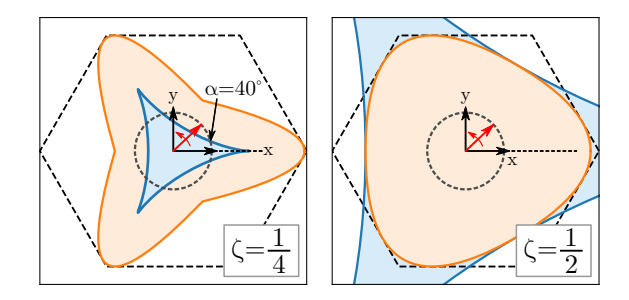


Fig. 10. Variable force angle (constant magnitude of $0.2F_{\rm max}$) trajectory for two bearings. These plots explain current discontinuities in Fig. 9.

Once the force magnitude reaches $0.2F_{\rm max}$, the currents in the bearing with $\zeta=\frac{1}{4}$ discontinuously jump to a new solution. This issue does not occur for the bearing biased at $\zeta=\frac{1}{2}$.

The discontinuity can be understood from the analysis framework of Section III-B based on when the force vector transitions between discriminant regions. This is depicted in Fig. 8, where the blue region 1 from Fig. 6 has been drawn on top of each bearing's maximum force profile (orange). In the case of $\zeta = \frac{1}{4}$, as the commanded force vector (shown in red) increases in magnitude, it passes out of region 1 at the force magnitude of $0.2F_{\text{max}}$. The discontinuity in Fig. 7 occurs at this location because the loss minimizing solution that was initially being commanded inside region 1 is no longer available and the controller must switch to the next lowest loss solution. This does not occur for the bearing with $\zeta = \frac{1}{2}$ because the larger ζ value expands the blue region 1 so that the bearing's force profile resides entirely within region 1. In other words, the commanded force never transitions between regions 1 and 2, and therefore the minimum L^2 solution is always feasible.

3) Variable angle force at $0.2F_{max}$: The two bearings from Section III-C2 ($\zeta=\frac{1}{4}$ and $\zeta=\frac{1}{2}$) are now investigated for a force trajectory where the magnitude is fixed at $0.2F_{max}$ but the angle is varied. The resulting current commands are shown in Fig. 9. The currents for the bearing biased at $\zeta=\frac{1}{2}$ are smooth and continuous, while the $\zeta=\frac{1}{4}$ bearing currents periodically jump between three of the four solution sets.

This behavior can again be understood from the framework of Section III-B. The trajectory of the commanded force vector is depicted in Fig. 10 as a dashed circle for each bearing. Several of the angles of the discontinuities in Fig. 9 correspond to where the force vector crosses the region 1

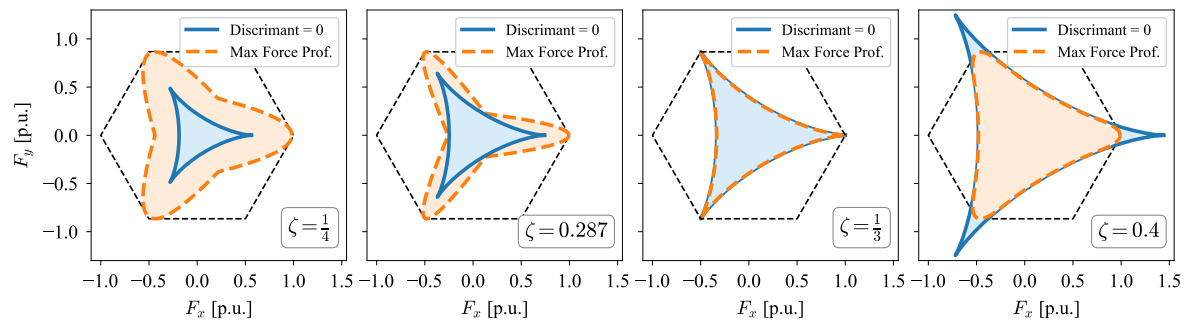


Fig. 11. The discriminant regions of several bearing designs (ζ values). Bearings with $\zeta \ge 0.3$ do not experience discontinuous current commands.

boundary in Fig. 10. As the force vector rotates in and out of the blue region, the minimum L^2 solution alternates between being feasible and infeasible, causing the cyclical current discontinuities. This behavior does not occur for the $\zeta=\frac{1}{2}$ bearing as the commanded force vector never leaves region 1. The remaining discontinuities occur at angles of 60° , 180° , and 300° that were identified in Section III-B as corresponding to a change in which region 2 solution yields the minimum L^2 norm.

D. Bearing Design Guidelines

As previously remarked, large discontinuities in the bearing coil currents over a smooth force trajectory can create problematic position regulator stability issues. It is therefore desired to eliminate these discontinuities from the exact force vector regulator. This can be accomplished by modifying the solution selection algorithm to avoid solutions that become infeasible for certain force vectors. However, based on the results of Section III-B, this would eliminate the use of the minimum L^2 solution, potentially resulting in an unreasonable increase in bearing power consumption. Alternatively, this can be addressed through careful bearing design. The possibility of this approach was revealed in the case studies of Section III-C, where bearings with $\zeta = \frac{1}{2}$ did not experience discontinuities. Design guidelines, in terms of values of ζ , are now developed to identify and evaluate bearings where the exact force vector regulator will not command discontinuous currents.

Section III-B showed that current discontinuities will not result when a commanded force vector remains in region 1 of Fig. 6. Inspection of Fig. 6 shows that the blue region 1 grows with ζ^2 , while both region 1 and the red hexagon (and therefore a bearing's maximum force profile—see Fig. 3) are proportional to $F_{\rm max}$. Consequently, as ζ increases, the blue region will grow relative to the force hexagon (and maximum force profile). This is depicted in Fig. 11 for various values of ζ . Key ranges for ζ can be identified as follows:

- 1) $\zeta = 0$: no current discontinuities, as the bearing's force profile will always reside in region 2 (the same number of solutions are always feasible), provided that the solution selection algorithm presented in [14] is utilized;
- 2) $0 < \zeta < 0.287$: current discontinuities will occur within the bearing's force profile as it spans regions 1 and 2;

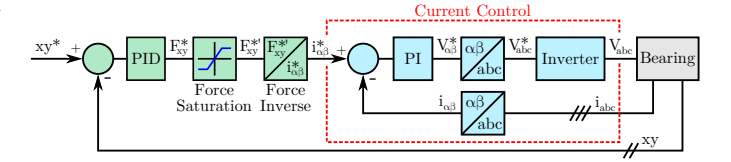


Fig. 12. Bearing control architecture; prime notation denotes saturated forces.

- 3) $0.287 \le \zeta < \frac{1}{3}$: no current discontinuities within the bearing's rated force profile², but discontinuities will occur when pushing past rated force to maximum force;
- 4) $\zeta \ge \frac{1}{3}$: no current discontinuities, as the bearing's force profile will always reside in region 1.

Based on these results, this paper proposes that three-pole bearings be designed with either $\zeta=0$ or $\zeta\geq\frac{1}{3}$. It was shown in [5] that these ranges of ζ are also preferred from a force density and ampere turns perspective, as can be seen in Fig. 4, with an optimal value of $\zeta=0.569$. This indicates that any practical three-pole bearing design can in fact be operated by the exact force regulator without concern for discontinuities (and corresponding stability issues) in the bearing currents.

IV. REGULATOR ARCHITECTURE AND IMPLEMENTATION

This section details the exact force vector regulator architecture and implementation for a real-time control platform. Fig. 12 shows a block diagram for controlling a three-pole bearing and consists of an inner current controller and an outer motion regulator. The current controller operates in the stationary α - β frame using a PI controller and can be realized following design principles that are well-understood in motor drives literature [27]. The motion regulator can be implemented as a PID controller following recommended practices for magnetic bearings, such as those provided in [4], [23]. The output of the outer loop PID controller is a force vector command that passes through a saturation block before being inverted into the i_{α} and i_{β} current commands of (6). The exact force vector regulator of Section III makes up the force inversion and saturation blocks of Fig. 12.

²Recall that the rated force profile is a circle with a radius equal to the inner radius of the maximum force profile–see Fig. 3.

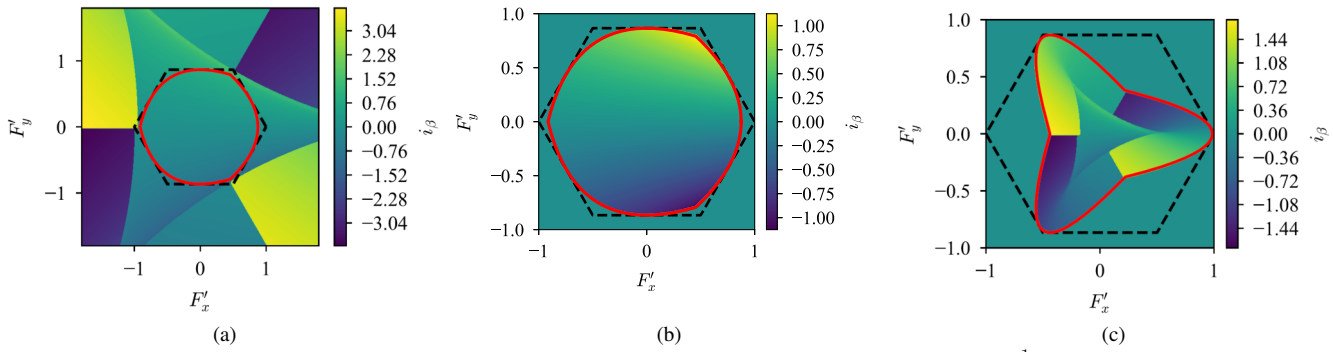


Fig. 13. i_{β} current maps for normalized bearings with (a) $\zeta =$ optimal; (b) $\zeta =$ optimal (zoomed in view); (c) $\zeta = \frac{1}{4}$.

A. Force Inversion

As previously discussed, calculating the control currents for a desired force vector requires computing the roots of a fourth order polynomial in the form of a depressed quartic (4). While various analytic methods exist for solving this type of equation (i.e., Ferrari's or Descartes solution), they are computationally expensive to perform in real-time. Several numeric methods also exist (i.e. computing the eigenvalues of a polynomial companion matrix [28]) but are often iterative, vary in terms of computational time requirements, and rely on the solution to converge. To avoid these complexities in a real-time control loop, it is proposed that the solutions be precomputed and interpolated using a lookup table. Various search algorithms exist that could be used to implement a lookup table efficiently; the well known binary search algorithm, for example, runs in logarithmic time [29].

Fig. 13a and 13b show non-dimensional β -axis current lookup tables for an optimally biased bearing (Fig. 13b is a zoomed-in view of Fig. 13a). The axes are the x and ycomponents of the desired normalized force vector and the contour color indicates the i_{β} current magnitude (computed as the minimum L^2 norm solution). A dashed black force hexagon and red maximum force profile are overlaid on the current map for reference. Note that an equivalent map must be constructed for the i_{α} current. It can be seen that the region 1 boundary discussed in Section III shows up naturally in the contours of Fig. 13a. Furthermore, distinct lines where the other expected current discontinuities will occur (60°, 180°, and 300°) show up on the contour plot but lie outside of the the maximum force profile, as expected for an optimally biased bearing. Fig. 13c shows the non-dimensional β -axis current lookup table for a bearing biased at $\zeta = \frac{1}{4}$. The region 1 boundary shows up naturally again in the contour plot, but because this bias level does not fall in the range of suggested bias fields ($\zeta = 0$ or $\zeta \ge \frac{1}{3}$), current discontinuities can be seen occurring within the bearing's realizable force profile.

The current maps depicted in Fig. 13 are normalized. To convert them to actual units, the force components and current values are multiplied by F_{\max} and $\frac{B_{\max}}{k_0}$.

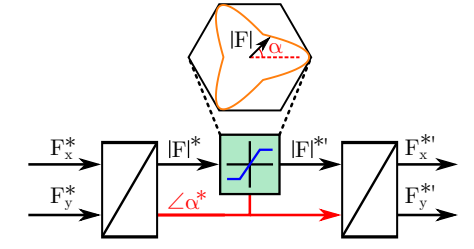


Fig. 14. Internal structure of the force saturation block shown in Fig. 12.

B. Force Saturation

It is necessary to saturate the force commands before they are inverted into current commands. This is done for two reasons, the first of which is to avoid discontinuous current commands that could occur from requesting a force that lies outside of the maximum force profile and therefore outside the accurate range of the lookup table interpolation of i_{α} and i_{β} . The second reason is to prevent the force inversion block from requesting currents that would produce airgap fields in excess of B_{\max} . These currents would presumably saturate the bearing steel and result in force vector error.

When saturating force commands, the force vector magnitude should be limited (as opposed to the individual components) because the maximum magnitude is dependent on the force vector angle α . Fig. 14 depicts how this can be done. First, the x and y force components are converted into a corresponding force magnitude and angle. The magnitude and angle are then used in a lookup table that contains the bearing's maximum force profile as a function of the force angle. The saturation block returns the minimum of the commanded input magnitude and the pre-computed maximum force profile for the specified force angle. The output magnitude and force angle are converted back into x and y components for use in the current lookup tables of the "Force Inverse" block.

V. VALIDATION

The proposed exact force vector regulator is now validated and compared to the conventional linear approach by studying the control implementation of an example bearing through both simulation and experimental results. The experimental results are obtained from a prototype CRAMB (see Fig. 2)

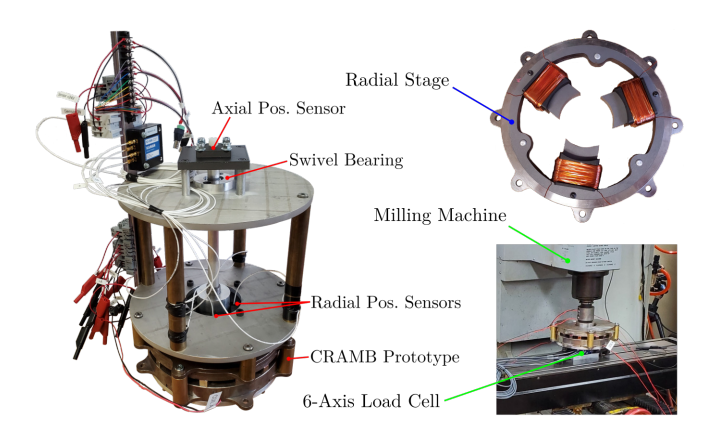


Fig. 15. Various views of the CRAMB prototype.

TABLE I CRAMB PROTOTYPE FIT PARAMETERS

Machine Parameter	Value
Unstable stiffness, k_{δ}	-129.9 N/mm
Coil R , L	1.88 Ω, 54.1 mH
$F_{\rm max},B_{\rm max}$	131.5 N, 0.8 T
k_1, k_2	205.45 N/T ² , 0.395 T/A

that implements the externally biased three-pole bearing as its radial stage (shown in Fig. 15). A mechanical swivel bearing allows the shaft end opposite the magnetic bearing to spin and pivot but constrains it from displacing radially. While the prototype is designed with an optimal bias field ($\zeta=0.569$), a compensation coil has been installed that can be re-purposed to modify the bearing's bias field when conducting static force tests. Full details of the prototype can be found in [5], [24]. Key machine parameters are provided in Table I, which includes the equivalent force model values needed to solve (4) and utilize the non-dimensional current map of Fig. 13b.

A. Simulation results

Bearing suspension instabilities that can result from using either the linear control approach or a poorly biased bearing are now investigated. Two bearing models are used for the simulations: 1) the bearing prototype of Fig. 15; 2) a reduced bias version of the prototype bearing with $\zeta = \frac{1}{4}$ (so that the exact force vector regulator will command discontinuous coil currents, as explained in Section III-D). These bearing models use the current maps of Fig. 13b and 13c with the machine parameter values listed in Table I. In all simulations, identical PID and PI controller gains (see Fig. 12) were used with a 700 Hz current controller bandwidth and 100V dc inverter bus.

1) Full motion control (startup and step disturbance): Fig. 16 shows the bearings' startup behavior and response to a 50 N step disturbance (at $t=1.5~\rm s$) for the exact and linear force regulators for two bias levels. For the optimally biased bearing, both controllers stably levitate the shaft from a touched down state. However, when the step force disturbance is applied, the force vector error of the linear force regulator causes the rotor to crash. For the $\zeta=\frac{1}{4}$ bearing, the linear force regulator is unable to even get the bearing to startup. The exact force regulator provides a stable startup but becomes

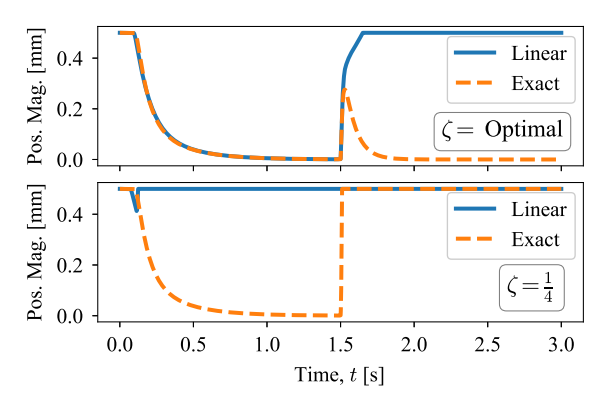


Fig. 16. Startup and response to a 50 N step disturbance directed at $\alpha=30^\circ$ for the exact and linear force regulators two bias values.

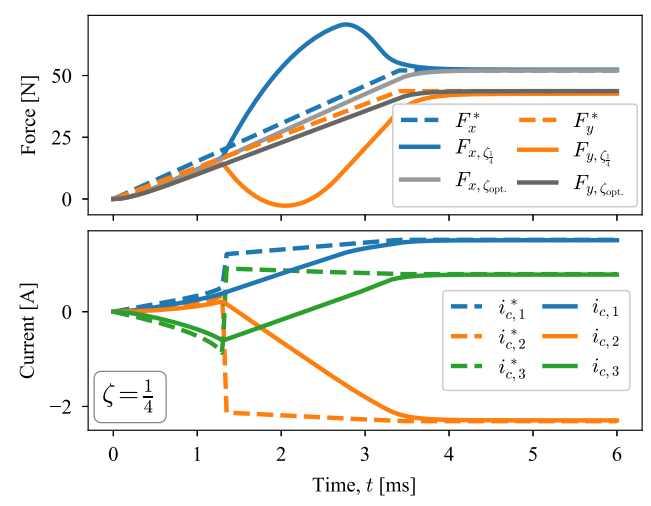


Fig. 17. Current discontinuities and force vector error that can result in a $\zeta = \frac{1}{4}$ bearing commanded to track a force ramp.

unstable after the force disturbance due to force vector errors resulting from discontinuous current commands.

2) 20 N/ms force ramp at 40°: The case study presented in Section III-C2 is now considered as a transient simulation to investigate the effects of discontinuous current commands. In this simulation, the motion controller is removed and an increasing force magnitude is directly commanded. The force results are depicted in the top of Fig. 17. The corresponding currents for the $\zeta = \frac{1}{4}$ bearing are shown in the bottom and reveal current commands similar to those depicted in Fig. 7. Notice that the optimally biased bearing is able to effectively track the force command. Initially, the $\zeta = \frac{1}{4}$ bearing also tracks the command effectively. However, when the commanded force vector crosses out of region 1 of Fig. 8, discontinuous currents are commanded and the slew rate of the three-phase currents is limited by the coil inductance and DC bus voltage. At this point, large force vector errors occur with angle errors over 40°. These large force vector errors can cause instabilities (i.e., Fig. 16).

3) 3600 RPM rotating force of $0.2F_{max}$: The case study presented in Section III-C3 is now considered as a transient simulation (again, with forces directly commanded and no motion controller). A force command of 26 N $(0.2F_{max})$ was

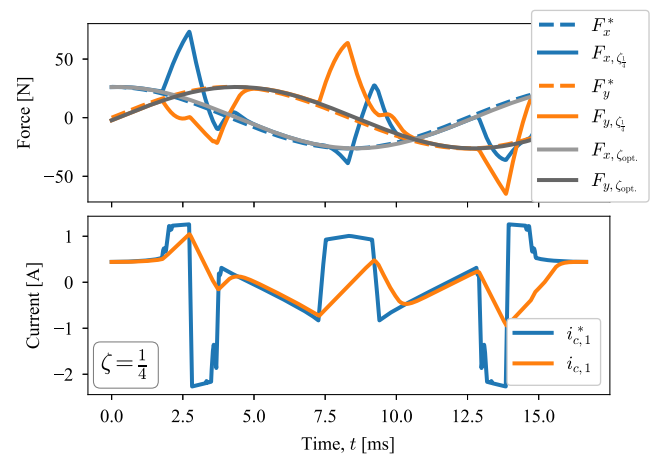


Fig. 18. Simulated results of 3600 RPM rotating force command to demonstrate vector error caused by discontinuous current commands when $\zeta = \frac{1}{4}$.

modeled as rotating at 3600 RPM (this is representative of force commands issued due to an unbalanced rotor). The results are shown in Fig. 18, where current commands correspond to Fig. 9. The controller is able to track the rotating force command in the optimally biased bearing, but not in the $\zeta=\frac{1}{4}$ bearing. This is due to the repeated discontinuities of the current commands and results in unacceptable force vector errors (over 150° angle error at times). Such large force vector errors appear as a positive feedback to the system and can result in instability. While it is common practice to suppress rotor imbalance compensation by rotating the shaft about its center of mass [4, sec. 8.3], this phenomenon will pose stability challenges by making the system sensitive to inacuracies in the imbalance control suppression and because such strategies are typically applied above a minimum threshold shaft speed.

B. Experimental validation

Three sets of tests were run on the prototype to validate the exact force vector regulator and compare its performance to the standard linear force regulator.

- 1) Static Force Test: The case study of Section III-C1 and Fig. 5b was investigated experimentally by applying the minimum L^2 coil currents of $\vec{i}_c = [i_{c,1}, -\frac{i_{c,1}}{2}, -\frac{i_{c,1}}{2}]$ and measuring forces produced. To complete this test, the CRAMB is placed in a commercial milling machine (right side of Fig. 15), with the rotor installed in the mill's spindle and the stator fixed to the mill's x-y table via a load cell. The test results are shown in Fig. 19, where it can be seen that the $\zeta = \frac{1}{4}$ profile matches Fig. 5b and has the expected minimum force value and corresponding coil current anticipated by the analysis framework of Section III-B and Fig. 6. Also as expected, the optimally biased bearing does not encounter a minimum force limit on this solution within its force profile.
- 2) Startup and Rotational Tests: The prototype machine was operated using the proposed exact force vector regulator at speeds up to 1300 RPM. The bearing startup event and the rotor orbit are shown in Fig. 20. Both tests demonstrate stable operating of the three-pole bearing.

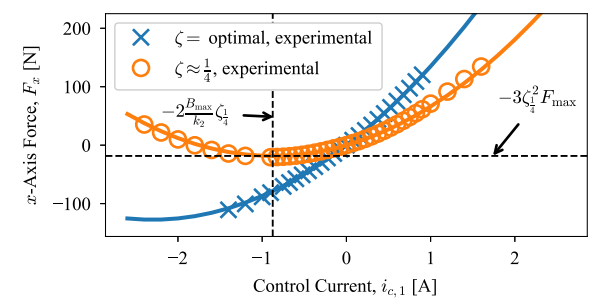


Fig. 19. Prototype quadratic force behavior for two bias levels.

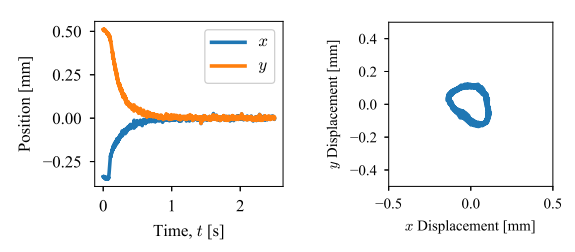


Fig. 20. Prototype startup (left) and orbit plot at 1300 RPM (right).

3) Force Vector Error Comparison Tests: Two tests were performed to compare vector error between the exact and linear regulators. First, a static test is preformed using the test stand configuration described in Section V-B1 where a constant magnitude force vector of 98 N was commanded through a range of force angles, while both regulator architectures were used to apply coil currents. Reaction forces were measured with the load cell (Fig. 21a) and the resulting vector error is depicted in Fig. 21b. The results show how effective each regulator is at obtaining the commanded force vector. The exact force regulator clearly achieves the highest performance, reducing the force magnitude and angle errors by over 20% and 9 degrees compared to the linear regulator.

Second, force vector error is observed during a levitation test. Prior to the test, a fixed force was applied to the levitating rotor by installing a tensioned elastic band connected to a rigid object. During the test, the bearing control architecture switches between using the exact and linear force vector regulators (the "Force Saturation" and "Force Inversion" blocks of Fig. 12 are replaced). The recorded data is shown in Fig. 21c, where the architecture change occurs at $t=4\,$ s. After a brief transient event, the currents return to their previous steady state values (as expected, because the force applied by the band has not changed), but the force commands converge to different final values. The difference between the steady state force command values demonstrates the force vector error of the linear regulator (the controller has to command an incorrect force vector to compensate for the disturbance).

VI. CONCLUSION

This paper develops a solution to one of the key challenges of externally biased three-pole bearings: force vector error that can cause instability in the magnetic suspension system. An exact force vector regulator is proposed that is able to eliminate this error between the force vector that a position regulator commands and the force vector that is actually produced on

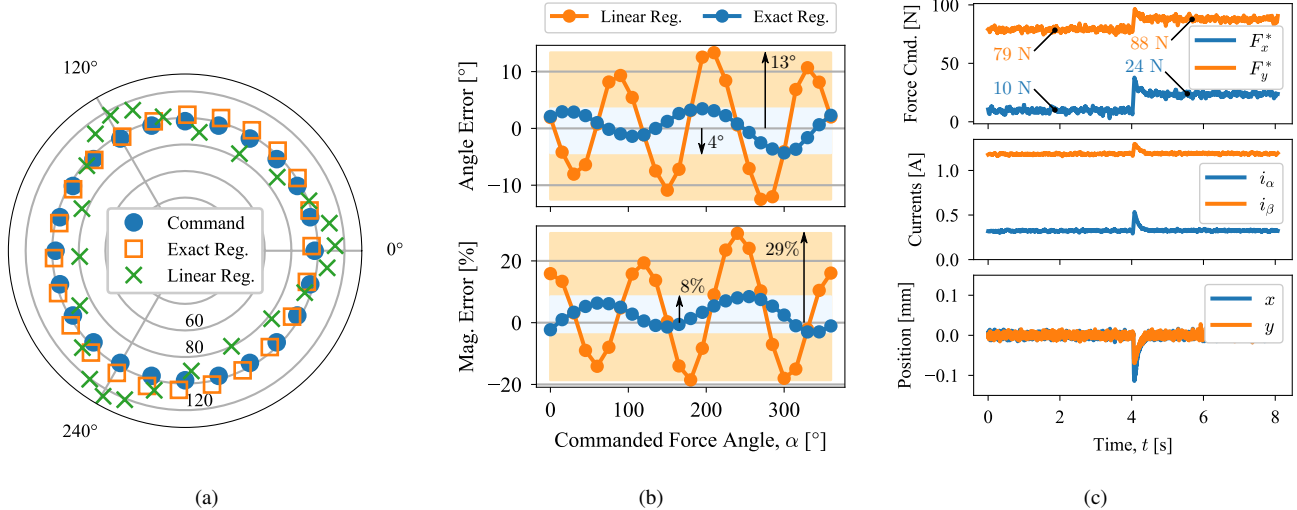


Fig. 21. Load cell measurements of (a) force vectors and (b) corresponding force vector error using an exact and linear regulator. (c) Levitation test data showing a transition from the exact to the linear force vector regulator with an 80 N constant force applied to the rotor.

the bearing's shaft. Graphical techniques are developed based around the discriminant of the bearing's force model in order to guide the bearing design process and explain discontinuous coil currents that the new regulator commands in poorly biased bearings. It is shown that bias field values that maximize the bearing's force density will also result in the best performance with the new force vector regulator. Practical implementation details for the new force regulator are provided and test results from a prototype bearing demonstrate its viability.

REFERENCES

- M. Kasarda, "An overview of active magnetic bearing technology and applications," *The shock and vibration digest*, vol. 32, no. 2, pp. 91–99, 2000
- [2] C. H. Park, S. K. Choi, and S. Y. Ham, "Design of magnetic bearings for turbo refrigerant compressors," *Mechanics & Industry*, vol. 15, no. 4, pp. 245–252, 2014.
- [3] J. Chen, J. Zhu, and E. L. Severson, "Review of bearingless motor technology for significant power applications," *IEEE Transactions on Industry Applications*, vol. 56, no. 2, pp. 1377–1388, 2020.
- [4] G. Schweitzer and E. H. Maslen, Magnetic bearings: theory, design, and application to rotating machinery. Springer, 2009.
- [5] N. R. Hemenway and E. L. Severson, "Three-pole magnetic bearing design and actuation," *IEEE Transactions on Industry App.*, 2020.
- [6] S. Eckhardt and J. Rudolph, "High precision synchronous tool path tracking with an amb machine tool spindle," in 9th International Symposium on Magnetic Bearings (ISMB), 2004.
- [7] S.-H. Park and C.-W. Lee, "Decoupled control of a disk-type rotor equipped with a three-pole hybrid magnetic bearing," *IEEE/ASME Transactions on Mechatronics*, vol. 15, no. 5, pp. 793–804, 2010.
- [8] W. Amrhein, W. Gruber, W. Bauer, and M. Reisinger, "Magnetic levitation systems for cost-sensitive applications—some design aspects," *IEEE Transactions on Industry Applications*, vol. 52, no. 5, pp. 3739– 3752, 2016.
- [9] M. Resinger, W. Amrhein, S. Silber, C. Redemann, and P. Jenckel, "Development of a low cost permanent magnet biased bearing," in 9th Int. Symposium on Magnetic Bearings (ISMB), Aug 2004, pp. 1–6.
- [10] M. Reisinger, H. Grabner, S. Silber, W. Amrhein, C. Redemann, and P. Jenckel, "A novel design of a five axes active magnetic bearing system," in *Twelfth International Symposium on Magnetic Bearings* (ISMB), Aug 2010, pp. 561–566.
- [11] S.-L. Chen and C.-T. Hsu, "Optimal design of a three-pole active magnetic bearing," *IEEE Transactions on Magnetics*, vol. 38, no. 5, pp. 3458–3466, 2002.
- [12] E. Fleischer and W. Hofmann, "Linear and nonlinear control of a three pole combined radial and axial active magnetic bearing-a comparison," *Mechanical Engineering Journal*, vol. 3, no. 1, pp. 15–00145, 2016.

- [13] D. C. Burgos, G. M. Sirbu, F. M. Porres, J. V. Landajuela, and L. F. Agorreta, "Pd control and sliding mode control using feedback linearization for 3-pole radial magnetic bearings of an energy storage flywheel," in 10th International Symposium on Magnetic Bearings (ISMB), 2006, pp. 1–6.
- [14] D. C. Meeker and E. H. Maslen, "Analysis and control of a three pole radial magnetic bearing," in *Tenth International Symposium on Magnetic Bearings (ISMB)*. Citeseer, 2006, pp. 1–7.
- [15] W. Hofman, "Behaviour and control of an inverter-fed three-pole active radial magnetic bearing," in *IEEE International Symposium on Industrial Electronics (ISIE)*, vol. 2, 2003, pp. 974–979 vol. 2.
- [16] J. Vadillo, J. M. Echeverria, I. Elosegui, and L. Fontan, "An approach to a 3-pole active magnetic bearing system fed by a matrix converter," in 11th International Symposium on Magnetic Bearings (ISMB), 2008, pp. 518–525.
- [17] X. Sun, H. Zhu, and T. Zhang, "Nonlinear decoupling control for 5 degrees-of-freedom bearingless permanent magnet synchronous motor," in 6th IEEE International Power Electronics and Motion Control Conference, May 2009, pp. 1842–1847.
- [18] E. Fleischer, S. Tröger, and W. Hofmann, "Control of a novel integrated radial-axial magnetic bearing," in *Thirteenth International Symposium* on Magnetic Bearings (ISMB), 2012, pp. 6–8.
- [19] H. Zhu, H. Chen, Z. Xie, and Y. Zhou, "Configuration and control for ac-dc three degrees of freedom hybrid magnetic bearings," in *Tenth International Symposium on Magnetic Bearings (ISMB)*, 2006.
- [20] J. Ju, H. Zhu, and C. Zhao, "Radial force-current characteristic analysis of three-pole radial-axial hmb," in 2016 IEEE Vehicle Power and Propulsion Conference (VPPC), Oct 2016, pp. 1–6.
- [21] R. Schoeb et al., "Radial active magnetic bearing for operation with a 3-phase power converter," in 4th International Symposium on Magnetic Suspension Technology, Gifu, Japan, 1997.
- [22] R. Schoeb, "Magnetic bearing apparatus and a method for operating the same," Oct. 10 2000, US Patent 6,130,494.
- [23] A. Chiba, T. Fukao, O. Ichikawa, M. Oshima, M. Takemoto, and D. Dorrell, Magnetic Bearings and Bearingless Drives. Newnes, 2005.
- [24] N. R. Hemenway, H. Gjemdal, and E. L. Severson, "New three-pole combined radial-axial magnetic bearing for industrial bearingless motor systems," *IEEE Transactions on Industry Applications*, under review.
- [25] E. Rees, "Graphical discussion of the roots of a quartic equation," The American Mathematical Monthly, vol. 29, no. 2, pp. 51–55, 1922.
- [26] S. Neumark, Solution of cubic and quartic equations. Pergamon Press, 1965.
- [27] D. W. Novotny and T. A. Lipo, Vector control and dynamics of AC drives. Clarendon Press, 2005.
- [28] R. Horn and C. Johnson, Matrix Analysis. Cambridge Univ Press, 1999.
- [29] E. Horowitz and S. Sahni, Fundamentals of Computer Algorithms. Computer Science Press, 1978.



Nicholas R Hemenway received a B.Sc. degree in mechanical engineering from the University of Wisconsin-Platteville, Platteville, WI, USA, in 2017, and a M.S. degree in mechanical engineering at the University of Wisconsin-Madison, Madison, WI. USA in 2020. His research interests include controls, multibody dynamics, electric machines, and magnetic levitation.



Eric L Severson (S'09-M'15) received the B.Sc. and PhD degrees in electrical engineering from the University of Minnesota, Minneapolis, USA in 2008 and 2015, respectively where he also worked as a post doctoral associate through 2016. He is currently an assistant professor at the University of Wisconsin-Madison.

Dr. Severson is an associate director of the Wisconsin Electric Machines and Power Electronics Consortium (WEMPEC) and fellow of the Grainger Institute for Engineering. His research interests in-

clude design and control of electric machines and power electronics, with focus areas in magnetic bearings, bearingless motors, flywheel energy storage, and off-highway vehicle electrification.

Dr. Severson is a recipient of the USA National Science Foundation CAREER Award in 2020, the Department of Defense NDSEG fellowship in 2009, and the National Science Foundation Graduate Research Fellowship in 2009.